#### **ORIGINAL PAPER**



# Design study of a camera system for Earth observation as a payload on the small satellite ROMEO

Dominik Starzmann<sup>1</sup> • Thorben Loeffler<sup>1</sup> • Jona Petri<sup>1</sup> • Damian Bargiel<sup>2</sup> • David Eidmann<sup>3</sup> • Michael Denk<sup>4</sup> • Christopher Conrad<sup>4</sup> • Sabine Klinkner<sup>1</sup>

Received: 16 February 2024 / Revised: 9 November 2024 / Accepted: 25 November 2024 / Published online: 28 December 2024 © The Author(s) 2024

#### **Abstract**

The importance of a safe food supply has increased due to climate change and its consequences. The number and severity of floods, droughts and plant diseases are rising which causes massive crop failures. Early and precise detection of plant diseases can lower crop failures as it enables early containment. Moreover, it promotes the targeted use of pesticides to protect the biodiversity. Satellite sensors improve the detection of plant diseases by enabling frequent and extensive vegetation observation. Hence, we present the design of a camera system for Earth observation on small satellites with a focus on the detection of plant diseases. The disease detection of sugar beets was chosen as the primary objective due to their importance for the German agriculture. This work is divided into two parts. First, the spectra of sugar beets are analyzed to determine spectral channels for a camera system. Second, a camera system is defined to capture spectral information within the previously defined wavelength ranges. The spectra of healthy and diseased sugar beets were measured in fields for agricultural research in Central Germany using a portable spectroradiometer. The investigated diseases are Cercospora leaf spot and virus yellows, which are among the most important pathogens worldwide. Based on the measured data, the so-called Normalized Difference Sugar Beet Index (NDSBI) is defined, which is a custom index to detect these diseases. We can prove that this index enables more precise detection of these sugar beet diseases than existing indices like the Normalized Difference Vegetation Index (NDVI). The camera system is designed as a payload for the small satellite Research and Observation in Medium Earth Orbit (ROMEO), which is being developed at the University of Stuttgart's (US) Institute of Space Systems (IRS). The proposed design fulfills the high radiation requirements as well as the system constraints of mass and volume. Three different options for the camera system are developed: two designs for the development at the US, one with lens optics and one with mirror optics, and an adjusted commercial camera system. All defined camera systems permit the measurement of the NDSBI to precisely detect sugar beet diseases.

Keywords Camera System · Small Satellite · Remote Sensing · Earth Observation · Vegetation Monitoring · Sugar Beet

Symbols			Abbreviations	
L	RadianceW/ $sr/m^2$	CDI	Cercospora Detection Index	
		CFRP	Carbon-Fiber-Reinforced Polymer	
		CLS	Cercospora Leaf Spot	
		CLSI	Cercospora Leaf Spot Index	
_		COTS	Commercial Off-The-Shelf	
$\bowtie$	Dominik Starzmann	DD	Displacement Damage	
	dominik.starzmann@irs.uni-stuttgart.de	FOV	Field of View	
1	University of Stuttgart, Pfaffenwaldring 29, 70569 Stuttgart,	GSD	Ground Sampling Distance	
	Germany	IRS	Institute of Space Systems	
2	Hochschule Geisenheim University, Von-Lade-Str. 1,	LEO	Low Earth Orbit	
	65366 Geisenheim, Germany	MEO	Medium Earth Orbit	
3	CORAmaps GmbH, Am Kavalleriesand 5, 64295 Darmstadt,	MTF	Modulation Transfer Function	
	Germany	NDMI	Normalized Difference Moisture Index	
4	Martin Luther University Halle-Wittenberg,	NDSBI	Normalized Difference Sugar Beet Index	
	Von-Seckendorff-Platz 4, 06120 Halle (Saale), Germany	NDVI	Normalized Difference Vegetation Index	



**NDWI** Normalized Difference Water Index

**OBDH** On-Board Data Handling

PRI Photochemical Reflectance Index

**ROMEO** Research and Observation in Medium Earth

Orbit

**SEE** Single Event Effects **SNR** Signal-to-Noise Ratio SoC System-on-Chip

SSO Sun-Synchronous Orbit

**TAPAS** Transmissions Atmosphériques Personnalisées

Pour l'AStronomie

TID Total Ionizing Dose TOA Top Of Atmosphere

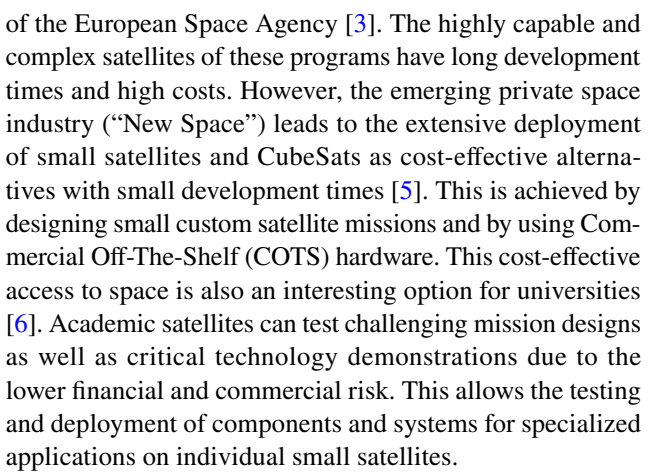
TRL Technology Readiness Level US University of Stuttgart

VY Virus Yellows

# 1 Introduction

Satellite-based camera systems are essential for many everyday applications. They play a key role in weather forecasting and regular mapping of the Earth to update navigation systems. In addition, these systems help to monitor natural disasters as well as the climate. Multispectral camera systems are necessary for many scientific purposes. Using different spectral channels enables the classification of various objects and surfaces [1]. Moreover, having wide-band spectral information about an object enables advanced analyses of it [1]. Both principles are applicable to vegetation. On the one hand, multispectral imaging is used to distinguish between different plants and on the other hand, the multispectral information facilitates the monitoring of the vitality of plants [2]. This principle is applied using the Normalized Difference Vegetation Index (NDVI), which is an index for general plant monitoring. It is based on the fact that the difference in reflection in the visible and near infrared spectrum changes depending on the crop's state of health and water content. This enables the detection of healthy and diseased plants and can be used in diverse fields of application. Farmers can improve their farming by using satellite data for precise fertilization and irrigation of their fields. Furthermore, a local application of pesticides is possible, which protects the biodiversity and improves the farming efficiency. Moreover, the findings can help on a global scale. For example, time series of vegetation monitoring data help to analyze climate change based on its effect on vegetation [3]. The importance of vegetation monitoring on a local and global scale increases as the consequences of climate change will become more severe during the next decades [4].

Multispectral satellite imaging on a global scale is mainly conducted by national space agencies as part of extensive Earth observation programs like the Copernicus Program



As of July 2023, there are over 6700 satellites in Earth's orbit [7]. Among these, 88% operate in the Low Earth Orbit (LEO) below 2000 km, while 9% operate in geostationary and higher orbits. The remaining 3% are distributed in the Medium Earth Orbit (MEO) with a majority located in the slot region between the inner and outer Van Allen radiation belts at an altitude of approx. 20,000 km. The University of Stuttgart's (US) Institute of Space Systems (IRS) is currently developing an academic small satellite mission called Research and Observation in Medium Earth Orbit (ROMEO) that targets to operate in the underutilized orbital regions above 2000 km altitude by using a cost-efficient design approach. Beyond that, the ROMEO satellite supports several payloads including a camera system. This offers the opportunity to develop, test and operate a customized multispectral camera system. As elaborated previously, vegetation monitoring is increasingly important, which is why this application was chosen. To improve current vegetation monitoring with general indices like the NDVI, a custom index called Normalized Difference Sugar Beet Index (NDSBI) is defined for specific crop monitoring of sugar beets. It enables more precise monitoring to improve the farming of a specific crop. The sugar beet is next to grain and canola one of the most common crop plants in Germany and it is the most important source of sugar in the northern hemisphere [8]. Therefore, it represents a suitable target for national, European and international satellite observations.

# 2 Custom Index Definition

## 2.1 The sugar beet

The sugar beet is a biennial plant of the amaranth family [9]. Its beet, which sprouts during the first year of the plant's life, has a high sugar content and is therefore used for sugar production. Around 50% of the global amount of sugar beets is produced in Europe [8] with Germany being the second largest sugar beet producer after France [10]. About 1.5



million hectares are cultivated with sugar beets in the EU [10]. Consequently, its cultivation is of great importance for the European agriculture, which is why satellite observations of sugar beets provide crucial information. Infections by pathogens are, next to droughts and floods, major causes of crop failures [4]. For the spectral analysis, it was focused on Cercospora Leaf Spot (CLS) and Virus Yellows (VY) disease. Cercospora is considered to be the most harmful pathogen for sugar beets [11]. It is a fungus that causes circular leaf spots with red-brown edges. This leaf damage can cause crop failures of up to 50% without proper treatment [12]. VY is caused by several viruses which are spread by aphids [13]. The relevance of this disease has increased during the last years due to the ban of neonicotinoids in Europe, which are effective insecticides against aphids to suppress the spread of viruses, but they are harmful to pollinators like bees [13]. This disease can also cause crop failures of up to 50% without proper treatment [12].

# 2.2 Methodology

## 2.2.1 Measurement campaign

The spectral field measurements were conducted on October 1, 2021, at sugar beet fields close to Northeim (Lower Saxony) and Wernigerode (Saxony-Anhalt) in Central Germany in close cooperation and agreement with Nordzucker AG. At the field close to Northeim, various test cells were designated to study the spread of CLS disease in sugar beet plants of different genotypes. In these test cells, no fungicide was applied. In comparison, VY was spread in designated test cells at a field close to Wernigerode, in which no corresponding crop protection products were applied. This experimental design allowed studying spectral properties of healthy plants as well as of sugar beets with varying degrees of the diseases. At this time of the growing period, the sugar beet plants in Northeim and Wernigerode showed well-expressed damage patterns.

The spectral measurements were conducted using a Spectral Evolution RS-3500 spectroradiometer [14]. The field portable instrument covers the wavelength range 350 nm to 2500 nm with a spectral resolution of 2.8 nm at 700 nm, 8 nm at 1500 nm and 6 nm at 2100 nm [14]. The instrument collects light via a fiber optic cable, which is then guided through dichroic beam splitters which guide the light through gratings that further split up the incoming radiation. Wavelength specific intensity values are then recorded using three detectors: a Si photodiode array covering the range 350 – 1000 nm, and two InGaAs photodiode arrays covering the wavelength ranges 1000 – 1900 nm and 1900 – 2500 nm. Spectral signatures were captured using two different measurement setups. The first setup was realized using the bare fibre optic with 25° Field of View (FOV) placed in

approximately 1 m distance above the ground, resulting in a diameter of the integrated spot of approximately 15 dm<sup>2</sup>. The calibration of the raw data into relative reflectance values was realized using a Zenith Lite<sup>TM</sup> reflectance standard of very high (approx. 95%) and homogeneous reflectivity. This setup was utilized to measure spectral signals that represent the sugar beet stock within the designated test cells representing different degrees of damage patterns and sugar beet genotypes. Several measurements were conducted per test cell and afterwards averaged. This approach results in mixed signals of sugar beet leaves and other plant parts as well as soil per test cell. Therefore, it generates spectra that are comparable to the mixed signals registered by imaging instruments for remote sensing from air and spacecraft. However, since the solar illumination serves as light source, such measurements are heavily affected by the atmospheric conditions during the spectra acquisition. As the weather conditions at the time of the field campaign in Wernigerode were partly cloudy, the resulting spectra were impaired by varying illumination conditions which could not be fully compensated even by taking the white reference in very short intervals.

A second measurement setup comprised measurements conducted with a contact probe and a leaf clip for specific measurements of leaves of different health conditions at the same test fields. The probe is equipped with an internal light source and allows contact measurements by integrating spectral information within approximate 1.5 cm in diameter. For each leaf, five measurements were conducted on the leaf surface as well as on the underside of the leaf. One healthy leaf and four leaves representing different damage levels in the different test cells were measured for both diseases. This setup provides spectra that are not affected by atmospheric conditions and recorded under stable illumination conditions. However, the spectral signatures represent solely the leaf spectra and are thus less comparable to remote sensing in which mixed signals are measured.

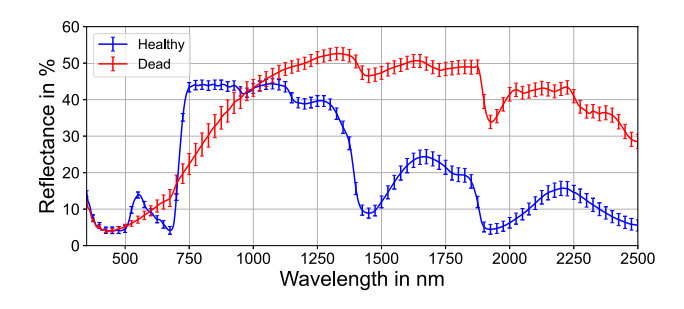


Fig. 1 Measured mean reflectance of a healthy (blue) and dead (red) sugar beet leaf



### 2.2.2 Analysis of the measured spectra

First, a healthy and dead leaf spectrum from the measurements are presented in Fig. 1. The former shows the typical sharp change ("red-edge") in reflectance in the range of 670 – 750 nm [15]. It is caused by the high absorption of the visual spectrum by chlorophyll and the high reflection of the near infrared spectrum in the leaf structure [16]. Hence, healthy leaves with high photosynthetic activity demonstrate a particularly sharp red-edge in their spectra. Moreover, the spectrum of the healthy leaf shows two minima around 1400 nm and 1900 nm, which are caused by water absorption [16]. The spectrum of the dead leaf looks different. The red-edge as well as the water absorption minima are hardly distinct as a result of the missing photosynthetic activity and the low water content.

As elaborated earlier, the contact measurements are well suited for the feature detection in the isolated leaf spectrum. However, these measurements vary across the leaf. Thus, averaging over the different measurements of the same leaf is necessary. The area measurements generate a mixed signal which is more representative for satellite observations but it is strongly influenced by the weather and the atmosphere and disease features are less distinct. Consequently, the contact measurements are analyzed first to determine the isolated leaf spectrum. A mean

spectrum is calculated for every leaf based on each contact measurement of the leaf. Then, the area measurements are analyzed with respect to the detected spectral features from the contact measurements. The different area measurements within one test cell are used to calculate a mean spectrum for each test cell.

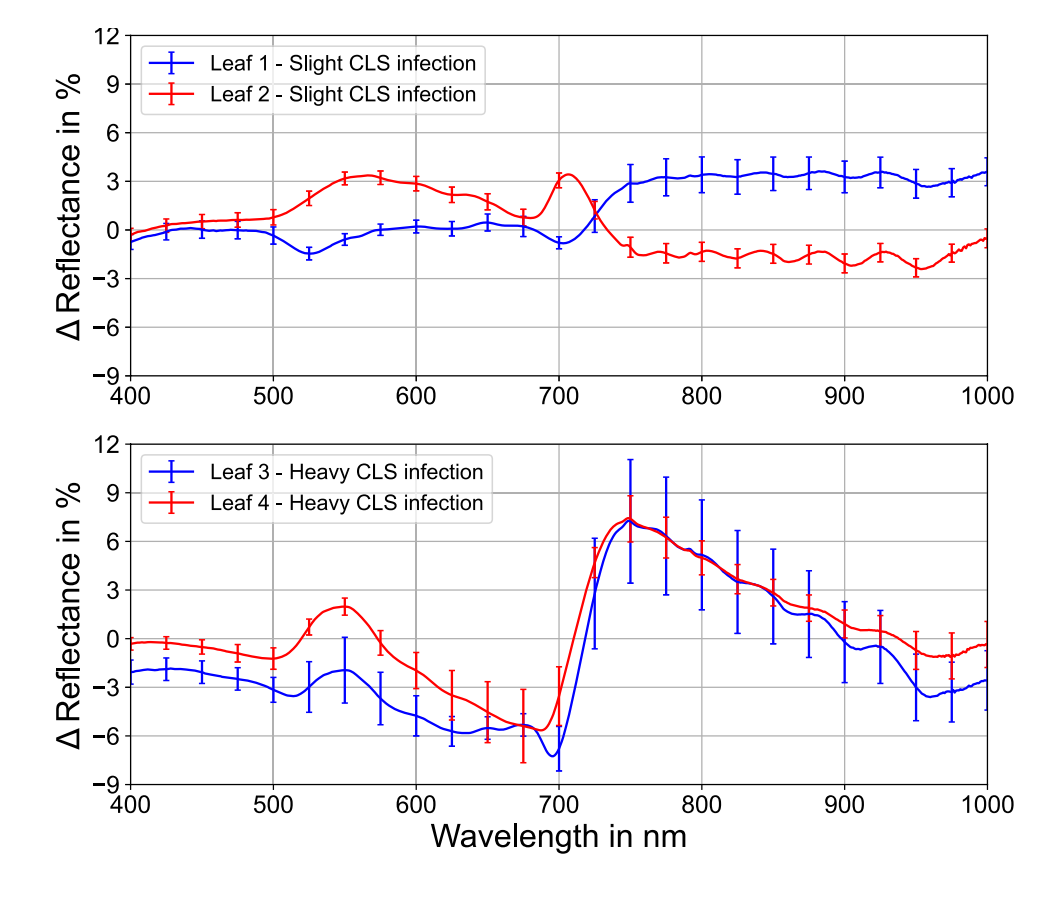
The average spectra of healthy plants are compared to spectra of diseased plants with different severity levels of the disease. The focus of the analysis is to detect the spectral bands with a high difference in reflectance which are suitable for an index definition. Higher differences in reflectance result in higher index differences, which improve the classification with the index. The spectrum analysis concentrates on the spectrum from 400 to 1000 nm due to the higher availability of camera components in this spectrum as well as the high variation of the atmospheric transmission beyond 1000 nm.

### 2.3 Results

#### 2.3.1 Results from the contact measurements

The calculated reflectance differences of four different leaves with CLS are presented in Fig. 2. Slightly infected plants show reflectance differences that can already be detected when the visual features of the disease are hardly distinct.

Fig. 2 Differences in reflectance of infected plants compared to healthy plants from contact measurements for a slight (up) and heavy (down) infection with CLS





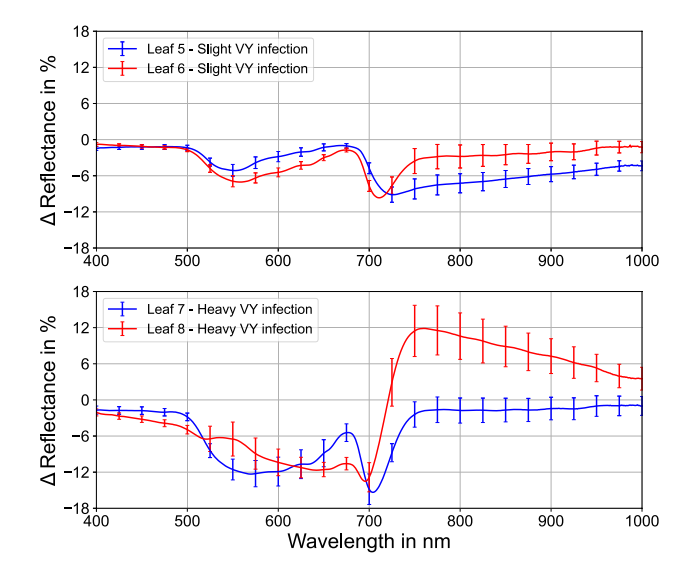


**Fig. 3** Differences in reflectance of infected plants compared to healthy plants from contact measurements for a slight (up) and heavy (down) infection with VY

However, these differences vary too much for the reliable detection of CLS. This changes with the increasing severity of the disease. Heavily infected plants have distinct differences which can be used for sufficient classification.

The reflectance differences for plants with VY are shown in Fig. 3. It can be seen that even slightly diseased plants feature differences in reflectance that are sufficient for a classification. Moreover, the differences of all plants with VY are larger than the differences with CLS.

To conclude, both diseases result in changed reflectances in the spectral range from 400 to 1000 nm. In particular, the spectral range from 500 to 700 nm and from 750 to 1000 nm are of great interest for spectral bands for an index.

## 2.3.2 Results from the area measurements

The results of the analysis of the area measurements are separated according to the different test cells in the test field. The differences in reflectance from the area measurements for plants with CLS are presented in Fig. 4.

The genotypes in test cell 1, 4 and 5 show the smallest deviations from the healthy sugar beet spectrum, which is why infections of these genotypes can hardly be detected. Test cell 2, 3, 6, 7 and 8 show distinct differences which enable a sufficient detection of the disease. The largest differences occur in the spectral range from 700 to 1000 nm, with maxima around 750-800 nm, which is therefore the most promising spectral range for a detection of CLS.

The differences in reflectance from area measurements for plants with VY are presented in Fig. 5. As mentioned in

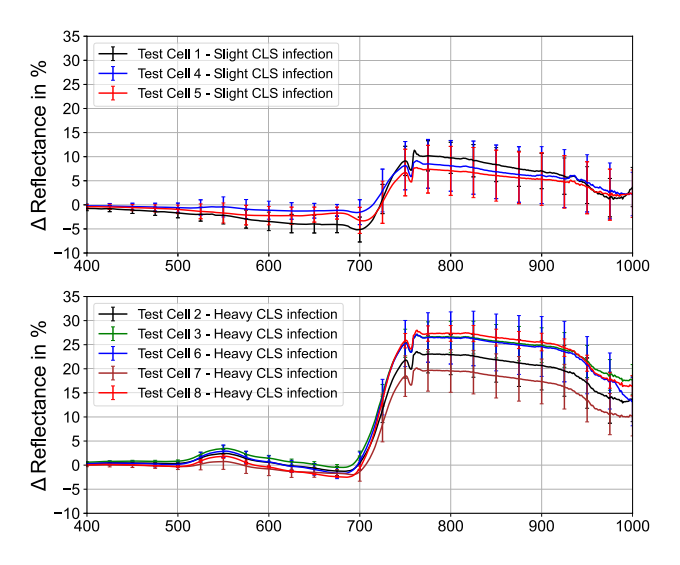


**Fig. 4** Differences in reflectance of infected plants compared to healthy plants from area measurements for a slight (up) and heavy (down) infection with CLS

section 2.2.1, the area measurements on the test field with VY are difficult to calibrate because of the varying illumination during the measurements. The large calculated differences can therefore only be partly related to the disease. However, differences in the spectral range 500-650 nm and 750-1000 nm are detected.

#### 2.3.3 Definition of the NDSBI

The spectral channels of the NDSBI are defined based on the presented analyses of sugar beet spectra. An index compensates effects that affect several spectral channels by forming a ratio, which for example equalizes the effects of shadows from clouds. Hence, the definition of the NDSBI is analog to the NDVI [2]. The goal is to achieve a sufficient differentiation of healthy and diseased plants with a small number of spectral channels, which ensures a feasible deployment on small satellites. Moreover, larger bandwidths are preferred to enable higher radiometric resolutions and shorter exposure times. The NDSBI is calculated using the radiances L of two spectral channels (Channel 1 and 2). The radiances are calculated by summing the measured spectral radiances over the spectral channel. The NDSBI is defined as follows:

$$NDSBI = \frac{L_{Channel2} - L_{Channel1}}{L_{Channel2} + L_{Channel1}}.$$
 (1)

The corresponding spectral channels are defined within the detected spectral ranges with high differences. They are optimized by iteratively varying the bandwidth for both channels in 10 nm steps starting with the minimum bandwidth of 30 nm to evaluate all possible combinations. Moreover, the



Fig. 5 Differences in reflectance of infected plants compared to healthy plants from area measurements for an infection with VY

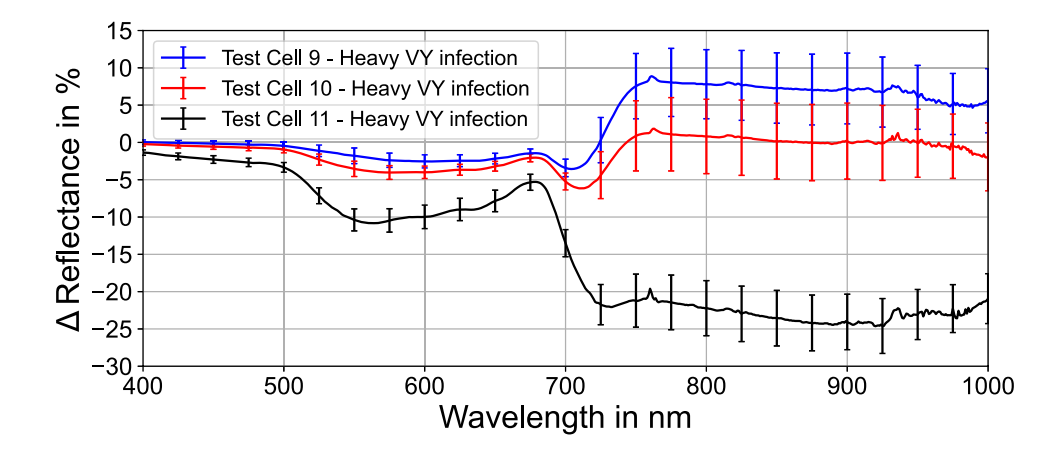


**Table 1** Calculated mean NDSBIs of CLS affected sugar beet plants and their differences to healthy plants with the spectral channels 620-700 nm and 750-780 nm

	Mean NDSBI	Mean difference
Healthy plants	0.538	_
Test Cell 1	0.133	0.405
Test Cell 2	0.176	0.362
Test Cell 3	0.186	0.352
Test Cell 4	0.350	0.189
Test Cell 5	0.296	0.242
Test Cell 6	0.032	0.506
Test Cell 7	0.135	0.403
Test Cell 8	0.075	0.464

**Table 2** Calculated mean NDSBIs of VY affected sugar beet plants and their differences to healthy plants with the spectral channels 620-700~nm and 750-780~nm

	Mean NDSBI	Mean difference
Healthy plants	0.674	_
Test Cell 9	0.347	0.326
Test Cell 10	0.357	0.317
Test Cell 11	0.291	0.382

area measurements with CLS are used for the optimization. The resulting channels are channel 1 from 620-700 nm and channel 2 from 750-780 nm. The calculated mean NDSBIs and their differences between healthy and infected plants for CLS and VY are presented in Tables 1 and 2.

To achieve a high degree of certainty for a reliable disease detection, the target minimum difference is set to 0.2. For CLS, the minimum mean difference is 0.189 and the average mean difference is 0.365. For VY, the minimum mean difference is 0.317 and the average mean difference is 0.342.

**Table 3** Calculated mean differences of infected plants compared to healthy plants for the indices from [17] for the area measurements with CLS

	Minimum Difference	Average Difference	Maximum Difference
NDSBI	0.189	0.365	0.506
NDVI	0.088	0.207	0.389
CLSI	0.038	0.091	0.118
PRI	0.020	0.035	0.044
CDI	0.008	0.021	0.041

The results in Tables 1 and 2 demonstrate that the NDSBI provides a good differentiation of healthy sugar beets and sugar beets with CLS or VY. All infected plants achieve higher differences than the minimum difference for a detection of 0.1. Furthermore, all test cells except for test cell 4 reach higher differences than the target minimum difference. Test cell 4 can still be sufficiently detected due to the high difference of 0.189. Additionally, the average mean differences widely exceed the target difference which promises a detection of the diseases independent of the genotype.

## 2.3.4 Performance of the NDSBI

The performance of the NDSBI is tested against several other indices. The following indices from [17] were used: NDVI, Cercospora Leaf Spot Index (CLSI), Photochemical Reflectance Index (PRI) and Cercospora Detection Index (CDI). The NDVI and PRI are indices for general vegetation monitoring and the CLSI and CDI are specific indices for CLS. Consequently, these indices are well suited for an analysis of sugar beet spectra. However, the indices in [17] are defined using a single wavelength. Therefore, they cannot be used for remote sensing as the bandwidth of 1 nm is too small. Nevertheless, these indices are used to determine the quality of the NDSBI. The indices and their differences



**Table 4** Calculated mean differences of infected plants compared to healthy plants for the Sentinel-2 indices [18] for the area measurements with CLS

NDSBI	Minimum Difference	Average Difference	Maximum Difference	
	0.189	0.365	0.506	
NDMI	0.115	0.320	0.540	
NDVI	0.031	0.079	0.147	
NDWI	0.034	0.065	0.121	

are calculated for the mean spectra of the area measurements with CLS. The results are shown in Table 3.

The calculated differences in Table 3 indicate that the NDSBI achieves a better detection of CLS than existing indices for the analysis of sugar beet spectra. All alternative indices feature minimum differences smaller than the minimum threshold of 0.1 for the detection of an infection. Moreover, only the NDVI provides an average difference which is suitable for a detection and can therefore be used as alternative. Nevertheless, the NDSBI demonstrates higher differences and hence superior performance.

Apart from that, the NDSBI is tested against indices that are already applied in space. For this reason, the NDVI, Normalized Difference Moisture Index (NDMI) and Normalized Difference Water Index (NDWI) from the Sentinel-2 mission are calculated [18]. These indices are less specific to sugar beets than the aforementioned indices but they are suitable for remote sensing because of their sufficient bandwidth. The NDVI and NDWI have a spatial resolution of 10 m while the NDMI has a resolution of 20 m. The calculated mean differences to healthy plants for CLS are printed in Table 4.

The NDVI and NDWI from the Sentinel-2 mission have minimum and average differences below the detection threshold of 0.1 and are therefore not suitable for a detection of CLS. However, the NDMI achieves differences that are above the threshold making it more suitable for the monitoring of sugar beets despite its lower spatial resolution. Its differences are smaller than the differences of the NDSBI which is why the latter demonstrates a better classification compared to the indices of the Sentinel-2 mission.

# 3 Camera System Design

## 3.1 The ROMEO mission

The idea of the ROMEO mission is to extend the current trend for reliable, high-performance, cost-effective and compact design of satellites into regions beyond the LEO. This endeavor necessitates the development of radiation-tolerant avionics capable of withstanding the particle flux of the inner radiation belt, which is predominantly characterized by highly energetic trapped protons [19]. Additionally, a green electrolysis-based water propulsion system [20] will be demonstrated to raise the apogee up to 2500 km. To ensure a natural de-orbit within 25 years, the perigee is simultaneously lowered below 330 km [21].

Besides the qualification of a radiation tolerant spacecraft in the MEO, the unique mission design enables various scientific payloads hosted on the ROMEO satellite: an earthshine telescope for Earth albedo measurements, particle detectors for space weather studies, a perovskite solar cells experiment, the demonstration of an adaptive high-speed data downlink system as well as camera systems for Earth observation [22]. The data generated by the payloads is processed by the central On-Board Data Handling (OBDH) system with a COTS System-on-Chip (SoC) which stores payload data in a non-volatile memory. The payload data is then transmitted to Earth via an adaptive data downlink that works in the X-Band with up to 150 Mbits<sup>-1</sup>. The main characteristics of the satellite platform are 82.5 kg system mass including 12 kg payload and 17 kg water as propellant. The dimensions of the launch configuration are  $545 \times 600 \times 682 \,\mathrm{mm}^3$ . The solar panels cover an area of  $180 \times 57 \,\mathrm{cm}^2$  in deployed state, resulting in an initial power generation of up to 250 W. The satellite will be three-axis stabilized with an absolute pointing performance of under 0.1°. The satellite is currently in the development phase C and its launch is planned in 2026. Further information on the ROMEO satellite can be found in [23].

# 3.2 Preliminary definition of the camera system

Besides typical environmental requirements in space, the ROMEO mission induces high radiation challenges. The satellite and its payloads have to resist a high Total Ionizing Dose (TID) and have to be tolerant against Single Event Effects (SEE) and Displacement Damage (DD). The requirements for the instrument from the ROMEO mission are summarized in Table 5. Moreover, the camera system shall measure the previously defined NDSBI for sugar beet observations. Therefore, it has to measure the two spectral channels of the NDSBI with a spatial resolution of maximum

Table 5 Requirements from the ROMEO mission

Maximum volume	$15 \times 15 \times 40 \text{ cm}^3$
Maximum mass	1.5 kg
Maximum power	5 W
Maximum data	$0.5~{ m GBd^{-1}}$
Lifetime	1 year
Radiation	$TID \ge 20 \text{ krad}$
Data interfaces	RS422, CAN, SpaceWire



**Table 6** Key parameters of the camera system based on the ROMEO mission requirements and scientific objectives

Pixel size	$4.5-10\mu m$
Focal length	270 – 600 mm
Aperture diameter	80 – 120 mm
Sensor format	1024 x 1024 pix – 2048 x 2048 pix
FOV	$0.98 \times 0.98 ^{\circ} - 1.96 \times 1.96 ^{\circ}$

Table 7 Cut-off angle of a baffle with 10 cm diameter and 1 ° FOV

Length	200 mm	100 mm	50 mm	20 mm
Cut-off angle	27.0°	45.2°	63.5°	78.7°

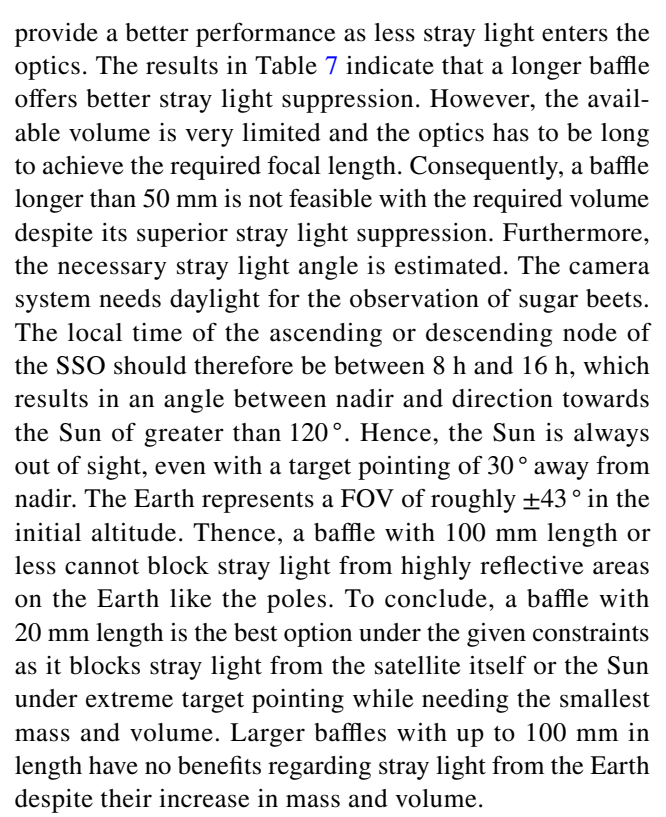
10 m and a temporal resolution of maximum 14 days. The spatial and temporal resolution ensure the local and early detection of the diseases.

# 3.2.1 Limitation of key parameters

The key parameters of the camera system can be limited based on the requirements from the ROMEO mission as well as the objective to measure the NDSBI with sufficient resolution. The camera system is designed for the initial orbit of the ROMEO mission which is a Sun-Synchronous Orbit (SSO) with 600 km altitude. Important key parameters are the focal length and pixel size. Their ratio is determined by the Ground Sampling Distance (GSD) of 10 m and the altitude of the orbit. On the one hand, a large focal length allows the use of larger pixels with higher capacity and therefore higher maximum Signal-to-Noise Ratio (SNR). On the other hand, it requires a large optics and hence high mass and volume. Moreover, possible aperture diameters are determined which also promote higher SNRs with larger and therefore heavier designs. The minimum aperture diameter for a given wavelength is determined by the Rayleigh criterion and has to consider an oblique view. The maximum diameter is determined by the given mass and volume requirements. Furthermore, the FOV is calculated which is dependent on the pixel size, number of pixels and the focal length. Consequently, the sensor format defines the FOV for a given pixel size and focal length. The preliminary limits of the key parameters are summarized in Table 6.

## 3.2.2 Preliminary component selection

Next, a preliminary component selection is done according to the previously determined key parameters and the requirements. First, possible baffles are investigated. For this reason, the cut-off angles of a baffle for several lengths with the mean preliminary diameter of 10 cm and a FOV of 1° are presented in Table 7. Smaller cut-off angles



One of the goals of the ROMEO mission is to promote the cost-effective design of small satellites, which requires the use of COTS components. Thus, only COTS camera sensors were considered. Moreover, only CMOS sensors on silicon basis are taken into account because of their high quantum efficiency in the relevant spectral range and their higher radiation tolerance compared to CCD sensors [24]. Additionally, the high orbital velocity and short exposure time necessitate a global shutter. The selection of a camera sensor has an important influence on the SNR. On the one hand, the quantum efficiency and the maximum capacity of the camera sensor are critical for the relevant signal. On the other hand, it is the component with the largest noise contribution next to the photon noise of the signal itself. The SNR is calculated using the following formula [25]:

$$SNR = \frac{Signal}{Noise} = \frac{\mu_{el}}{\sqrt{\mu_{el} + Read_{el}^2 + Dark_{el}^2}}$$
(2)

The signal is determined by the generated electrons  $\mu_{el}$ . The noise is calculated using the three main noise contributors: photon noise, readout noise and dark noise. The signal and photon noise for the preliminary SNR are calculated using known radiances for three spectral channels in the relevant spectral range from previous work at the US [25]. The exposure time is calculated under the constraint that the maximum allowed offset during the exposure is one pixel which



**Table 8** Calculated ranges of the SNR due to different camera sensors for three channels for vegetation [25] with an exposure time of 1.32 ms and 10 cm aperture diameter

Spectral channel	Summer (clear)	Summer (dusty)	Winter (dusty)
Green	50 – 57	25 – 35	16 – 26
Red	38 - 55	20 - 36	13 - 28
Near infrared	94 - 170	68 - 131	52 - 108

is equivalent to an offset of the GSD on the ground for nadir pointing. Therefore, the maximum exposure time is 1.32 ms for the orbital velocity of roughly 7.6 km s in the initial orbit. The calculated SNRs dependent on the sensor are presented in Table 8

The results in Table 8 state that the camera sensor has crucial influence on the SNR which increases for longer wavelengths. Hence, the use of sensors with high quantum efficiency in particular for high wavelengths is beneficial. Based on the mentioned criteria, 18 potential COTS camera sensors can be found. The four camera sensors that fit best are: Sony IMX 174, Sony IMX 566 (2x2 binning), Sony IMX 430 and ams CMV 4000.

This preliminary selection of camera sensors features pixel sizes from  $4.5\,\mu m$  to  $5.86\,\mu m$ . As mentioned before, this determines the focal length of the optics. The optics has a strong influence on the relevant signal and hence the SNR as it determines the incident light with its f-number and transmission quality. The resulting parameters of the optics from the sensor and baffle selection based on the key parameters and requirements of the camera system are listed in Table 9. A market research indicates that only custom optics are available with these parameters and mission constraints.

The Modulation Transfer Function (MTF), which is a measure for the resolution and contrast of an optical system [26], for an ideal optics with spherical aperture is calculated to determine the expected optical performance. The calculation of MTFs for several focal lengths in the relevant spectral range with a fixed aperture diameter of 10 cm demonstrates that a larger focal length results in a smaller MTF and hence less contrast. Further analysis shows that the MTF improves for larger aperture diameters. It is also important to mention that the MTF of a real optics is always worse than the ideal MTF due to aberrations. Taking this

Table 9 Preliminary parameter limits of the optics

Aperture diameter	80 - 120  mm	
Focal length	270 – 444 mm	
Spectral range	400 – 1000 nm	
Maximum volume	ø 130 mm x 330 mm	
Maximum mass	1 kg	

into account, the expected maximum MTF for pixel sizes from  $4.5 \,\mu\text{m} - 5.86 \,\mu\text{m} (111 \,\text{lpmm} - 85 \,\text{lpmm})$  is 0.4.

The high radiation environment of the ROMEO mission is also challenging for the optics. On the one hand, ionizing radiation lowers the transmission of glass which leads to reduced SNRs [27]. Therefore, the custom lens optics for the ROMEO mission is designed using radiation resistant optical glasses which are stabilized by adding cerium [27]. On the other hand, proton radiation, which is particularly important in the MEO, changes the refractive index and density of glass which leads to aberrations [28]. Hence, sufficient margin to the diffraction limit of the optics is foreseen.

## 3.2.3 Orbit analysis

The temporal resolution is crucial for time series and reliable observation of certain areas. It is determined by the number of passes and the time between passes, which are highly dependent on the orbit. As described previously, the ROMEO satellite has a water propulsion system and will therefore change its orbit during the mission. The mission can be divided into three phases: initial orbit, transfer phase and final orbit. The initial orbit is a SSO with an altitude of 600 km. During the transfer phase, this SSO changes gradually to an elliptical orbit with an apogee of 2500 km and perigee of 330 km. This phase is investigated using four orbits from the ephemeris during the transfer phase with increasing apogee (1000 km, 1500 km, 2000 km, 2500 km). The calculations for the last phase are done using the last orbit of the orbit transfer. The passes are simulated for a sugar beet field next to Hildesheim, a city in Germany in a region with high agricultural importance. The simulations are conducted for several minimum elevations which implies different nadir angles for the satellite. The calculated number of passes for each phase are presented in Table 10.

The results demonstrate that a larger nadir angle leads to a higher number of passes. However, this results in a higher slant range which increases the GSD. Moreover, the footprint of the images changes due to the tilted observation. Consequently, a better temporal resolution leads to a worse spatial resolution and vice versa. The results also show that the transfer phase and the resulting final orbit feature a worse temporal resolution than the initial

**Table 10** Calculated number of passes depending on the nadir angle with a maximum distance of 1000 km

Nadir angle	10°	20°	30°	Duration
Initial orbit	21	42	68	3 Months
Transfer phase	40	50	68	6 Months
Final orbit	12	24	39	3 Months
Total	73	116	175	12 Months



orbit. Nevertheless, the orbit analysis proves that images of specific locations can be taken at least every two weeks during the whole mission with reasonable degradation of the spatial resolution. But it also indicates that nadir pointing is not sufficient to achieve an adequate temporal resolution. Moreover, it is important to mention that the transfer maneuver changes the imaging geometry. The illumination hardly alters at the beginning of the mission due to the SSO. This changes for the elliptical orbit caused by the transfer maneuver. The illumination can then vary between every measurement which impedes the comparison of measurements.

Additionally, it is planned to calibrate the camera during the mission. Flat field correction is done by imaging homogeneous areas on Earth like deserts particularly in polar regions. As no mechanical shutter is foreseen, the dark field correction uses dark areas in the sky like the Hubble deep fields [29]. The inclination of the ROMEO trajectory will not be actively changed during the mission which is why both, polar regions as well as the Hubble deep fields, are visible during the whole mission. Moreover, drone images of sugar beet fields in Germany and Sentinel-2 images can be used for the radiometric calibration of the NDSBI. The in-orbit calibration is necessary to ensure radiometric stability as the performance of the optics and electronics will degrade during the mission, in particular due to the high radiation. However, the NDSBI uses the ratio of two spectral bands which is why less radiometric stability is required compared to absolute measurements.

## 3.3 Custom camera system design

## 3.3.1 System architecture

First, the system architecture for the custom camera design is chosen. Possible system architectures for multispectral imaging and their evaluation for the ROMEO mission are presented in Table 11. Two concepts pose reasonable

**Table 11** Evaluation of diverse architectures of camera systems for multispectral imaging

Architecture	Feasibility	Reason
Butcher block filter	Yes	
Beam splitter	Yes	
Line scan sensor	(Yes)	Target pointing
Multi-layer sensor	No	Spectral resolution
Separate cameras	No	Mass & volume
Mosaic filter	No	Spatial resolution
Filter wheel	No	Mechanics

architectures: a camera with butcher block filter and a camera with a beam splitter. On the one hand, the architecture with beam splitter has operational advantages as it records both spectral channels with the full FOV while the architecture with butcher block only covers one half of the FOV per channel. On the other hand, the former needs more electronics as well as more mass and volume. However, the operational advantage cannot justify the increase in resources which is why the architecture with butcher block filter is chosen.

## 3.3.2 Component selection

Second, the components for the custom camera design are selected. As mentioned before, the optics needs to be a custom optics as no suitable COTS optics is available. The parameters of two custom optics, one with lenses and one with mirrors, as well as the resulting system parameters are summarized in Table 12. The mirror optics includes efficient internal baffles while the lens optics needs an additional baffle with the aforementioned length of 20 mm with low stray light suppression. According to optics manufacturers, a focal length of 350 mm is considered to be the maximum possible focal length under the given physical constraints. The system parameters are calculated using the results of the selection of the camera sensor, electronics box and structural components which are described in the following.

The focal length of 350 mm reduces the number of possible camera sensors from section 3.2.2 as sensors with pixel sizes larger than 5.86 µm cannot reach the required GSD. All remaining sensors have comparable technology readiness levels (TRL) and costs. The final sensor trade-off is hence based on the following criteria: pixel size, full well capacity, noise, quantum efficiency and quantization. This trade-off results in the Sony IMX 430 being the best option for the

**Table 12** Preliminary parameters of the custom lens and mirror optics and the resulting system parameters

	Lens optics	Mirror optics
Focal length	350 mm	350 mm
Length	300 mm	210 mm
Diameter	80 mm	130 mm
Optics mass	1.5 kg	1.7 kg
MTF	> 0.3@ 111 lp/mm	> 0.3@ 90 lp/mm
Cut-off angle	±79°	±5°
System volume	$12 \times 12 \times 40 \text{ cm}^3$	$15 \times 15 \times 30 \text{ cm}^3$
System mass	2.15 kg	2.30 kg
System power	2–3 W	
System data	$0.5{\rm GBd^{-1}}$	
Data Interface	RS422	



ROMEO mission due to its small pixel size for a high spatial resolution and its high quantum efficiency with low noise. It features a radiometric resolution of 12 bit with a full well capacity of 25,000 electrons which results in a sufficient maximum SNR of 158.

Moreover, the camera system requires electronics for the operation of the camera. The mass and volume of the electronics box are estimated using the payload cameras of the previously mentioned research at the US on the satellite Flying Laptop [25]. Based on its cameras, the electronics box has an estimated mass of 0.4 kg and volume of 80 x 80 x 80 mm<sup>3</sup>. Several measures are implemented to reduce the radiation seen by the electronics. The main structure of the ROMEO satellite consists of six-layer Carbon-Fiber-Reinforced Polymer (CFRP) sandwiches with aluminum honeycomb cores which reduce the TID inside the satellite to 15 krad [23]. By combining a 3 mm aluminum sheet with a 9 mm epoxy resin layer for the electronics casing, the TID seen by the electronics is further reduced below 5 krad [23]. Additionally, it is planned to power off the camera during periods with high radiation exposure which significantly reduces the damage by SEE [23]. The measurement of the NDSBI requires a small GSD which can only be reached in the LEO which is why the camera is powered off in the MEO and in case of solar particle events.

## 3.3.3 Accommodation on the ROMEO satellite

An initial thermal and structural assessment for the integration of the camera on the ROMEO satellite has been conducted. The structural components are designed analog to the payload cameras of the Flying Laptop, which represents a flight proven heritage design [25]. The structural components for the accommodation consist of two optical benches made of sandwich structures with face sheets of CFRP and an aluminum honeycomb core. These sandwich structures feature a high stiffness, low thermal expansion and low density. The resulting designs for both optics are presented in Fig. 6.

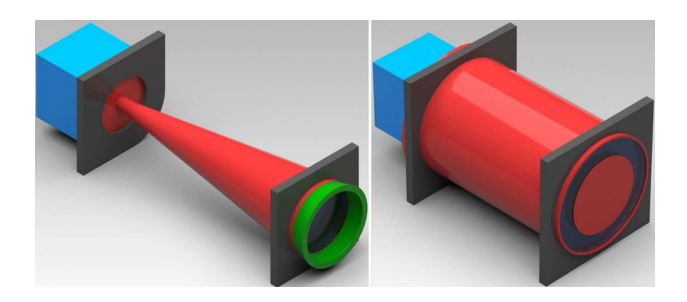


**Fig. 6** Camera design with lens optics (left) and mirror optics (right) - Components: Optics (red), electronics (blue), structure (black) and baffle (green)

The initial thermal analysis of the ROMEO satellite results in a temperature range of the camera from -25 °C to 10 °C. The required temperature range is -40 °C to 60 °C. Hence, the required temperature range is met by the camera. The simulated temperatures are in the lower range of the allowed temperature range which is beneficial for the image quality because of the lower dark current. On the one hand, the coldest temperatures are reached when the satellite is in safe mode as a result of the low dissipation and therefore low temperatures of the complete satellite. On the other hand, the highest temperatures occur during maneuvers. The dissipated heat of the thruster itself but also the high dissipation of the other components result in an overall warm satellite structure which is why most components including the camera experience the highest temperatures in this case.

## 3.3.4 Performance

First, the camera system is evaluated looking at its scientific performance, which is determined by the SNR and the classification of diseased sugar beets with the NDSBI. In section 2.3.3, the NDSBI was defined based on the measured spectra without considering technical constraints of a camera system. However, specific adjustments of the spectral bands can compensate for technical constraints and therefore yield higher performances. The analysis of all parameters of the SNR calculation reveals that the quantum efficiency of the camera sensor is the only technical parameter that has crucial influence on the spectral band selection. Moreover, the definition of the NDSBI is based on radiances measured 1 m above the field without relevant atmospheric absorption. Consequently, the Top of Atmosphere (TOA) radiances have to be calculated which is done by using atmospheric transmissions from Transmissions Atmosphériques Personnalisées Pour l'AStronomie (TAPAS) [30]. The optimization of the spectral channels with the TOA radiances and the quantum efficiency of the sensor analog to the optimization in section 2.3.3 results in a slight change of channel 1 to 580 – 690 nm. Channel 2 remains unchanged despite the transmission minimum of the atmosphere around 760 nm. All mean differences between healthy and diseased plants for this custom NDSBI\* are above the threshold of 0.2. It achieves better results than the general NDSBI and is therefore used for the camera system. Overall, the expected differences promise a good detection of the investigated sugar beet diseases. The resulting SNRs for the two spectral channels of the custom NDSBI\* with the TOA radiances are presented in Fig. 7.

It is crucial that the SNR is high enough for the scientific utilization of the camera measurements. The recommended threshold for scientific observations is 100 [25]. The maximum SNR of 158 is determined by the full well capacity of the camera sensor. Figure 7 demonstrates that the target



Fig. 7 SNR for both channels of the NDSBI\* with the TOA radiances of sugar beets for the custom camera designs

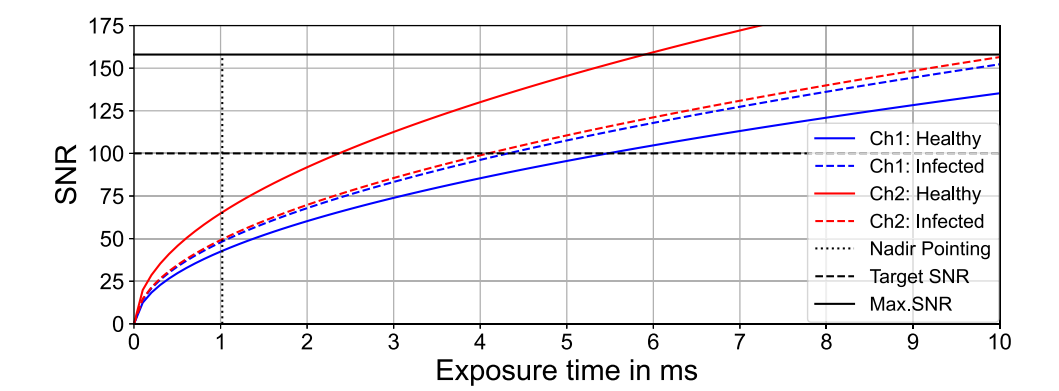


**Table 13** Important performance parameters in the initial orbit for both custom camera designs

GSD (nadir)	7.7 m
GSD (target pointing)	10.3 m @ 30°
Imaging area	12.59 km x 9.63 km
Swath	12.59 km
FOV	1.20 ° x0.92 °
Spectral channels	580 – 690 nm
	750 – 780 nm

SNR can be reached with exposure times from 2 to 5 ms. However, the maximum exposure time of 1.02 ms with nadir pointing in the initial orbit results in SNRs from 50 to 70. Consequently, target pointing is necessary for images with higher SNRs. Apart from that, a high SNR with nadir pointing can be reached by taking several images with a high frame rate and superposing these images. The key performance parameters of both custom camera designs are summarized in Table 13. All in all, it can be shown that images with high SNR and sufficient spatial resolution are feasible, which enable adequate scientific measurements of the NDSBI\*.

# 3.4 Commercial camera systems

Commercial camera systems are also considered next to the previously presented custom camera designs. Roughly 20 suppliers of camera systems for space applications were found during a market research. From these suppliers, only three cameras partly comply with the requirements in Table 5 while achieving the necessary GSD. These are the HyperScape 100 and MultiScape 100 from Simera Sense [31] as well as the 90 mm camera from KairoSpace [32]. However, the peak power of both cameras from Simera Sense is higher than the required maximum power. Moreover, these cameras use a line sensor instead of an area sensor, which induces operational constraints. Hence, the 90 mm camera is the only commercial camera to fully comply with all requirements after several adjustments, which

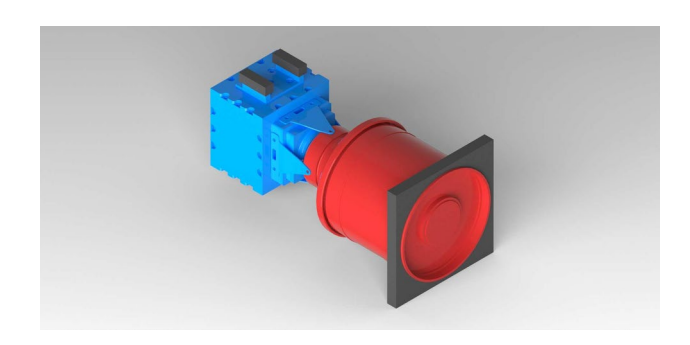


Fig. 8 Adapted 90 mm camera from KairoSpace [32] - Components: Optics (red), electronics (blue), structure (black)

**Table 14** Key parameters of the adapted 90 mm camera from Kairo-Space [32] in the initial orbit

System volume	$10.8 \times 10.8 \times 24.3  \text{cm}^3$
System mass	1.4 kg
System power	4.2 W
System data	$0.5\mathrm{GBd^{-1}}$
Data Interface	RS422
GSD (nadir)	4.5 m
GSD (target pointing)	6.0 m @ 30°
Swath	14.9 km
FOV	1.5°

are described in the following. Therefore, it demonstrates a reasonable alternative to the custom camera designs. The design of the adapted 90 mm camera is presented in Fig. 8.

Several adjustments are necessary for a deployment of the 90 mm camera on the ROMEO satellite, which were elaborated in cooperation with KairoSpace. The camera needs to measure the two spectral channels of the NDSBI\*. This is attained by adding a butcher block filter. Moreover, structural elements for a proper accommodation of the camera inside the ROMEO satellite are necessary. For this reason, an optical bench as described in section 3.3.3 is added. The electronics box already features mounts which are adapted



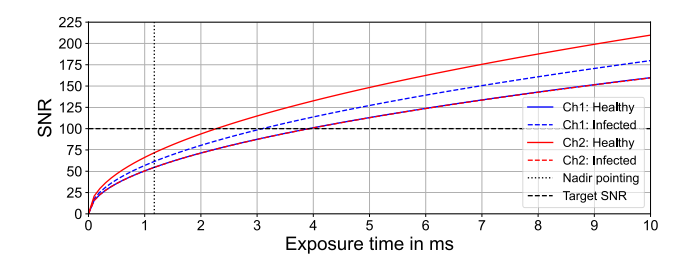


Fig. 9 SNR of the 90 mm camera with 2x2 binning for both channels of the NDSBI\* with the TOA radiances

to the ROMEO satellite by the manufacturer. Moreover, the commercial camera system requires the same temperature range as the custom camera designs which is therefore also met by the simulated temperatures described in section 3.3.3. The key parameters of the adapted camera are summarized in Table 14.

Finally, the achievable SNR with the 90 mm camera is analyzed analog to section 3.3.4. The 90 mm camera has a radiometric resolution of 14 bit with a full well capacity of 18000 electrons. This results in a maximum SNR of 134 which is sufficient for the required SNR of 100. First results indicate that the SNR of roughly 25 with nadir pointing is insufficient. This is mainly caused by the small exposure time of 0.59 ms due to the small GSD. However, this can be avoided by using 2x2 binning. Even with binning, the camera system achieves a sufficient GSD of 9 m, which results in a longer exposure time and higher full well capacity and therefore significantly higher SNR. Hence, it is possible to choose between high spatial or high radiometric resolution during the operation of the camera. The calculated SNRs with 2x2 binning are presented in Fig. 9. They are higher than the SNRs simulated for both custom camera designs. Nevertheless, nadir pointing is not sufficient to achieve the target SNR of 100. This can be reached with exposure times from 2 to 4 ms.

## 4 Conclusion

First, spectra of healthy and infected sugar beets with CLS or VY disease were measured. The analysis of these spectra shows that both diseases cause differences in the leaf spectrum with the highest differences in the spectral ranges 500 - 700 nm and 750 - 1000 nm. Further analysis results in 620 - 700 nm and 750 - 780 nm being the best two spectral channels for the NDSBI, a custom index to detect these diseases. Moreover, the comparison with existing indices for sugar beets as well as indices of the Sentinel-2 mission demonstrates that the NDSBI achieves superior performance on the detection of the investigated diseases.

Second, a camera system is defined to measure the NDSBI. Initially, the design demonstrates that the planned measurements are feasible within the requirements of the ROMEO mission by limiting the key parameters and components and by analyzing the orbit. Then, two custom camera designs are developed which can achieve the mission goals and comply with the requirements except for the allowed system mass. Furthermore, a market research identifies a commercial camera system that complies with all requirements with several adjustments. It is the best option as secondary payload of the ROMEO satellite due to its smaller mass and volume as well as higher resolution besides a higher TRL.

To conclude, this work demonstrates that specialized indices deployed on custom or commercial cameras on small satellites have the potential to outperform comprehensive Earth observation programs on certain tasks. The developed camera system enables the regular, large-scale and precise monitoring of sugar beet diseases by measuring the NDSBI. Due to the consequences of climate change, an increased spread of diseases is expected, which results in crop failures and necessitates for extensive application of pesticides [4]. As this can be significantly limited by using the data of this camera system, it promises an important contribution to the agricultural economy and biodiversity.

Author contributions The work was presented at DLRK 2023 by D.S.. D.S. wrote the main manuscript text, conducted the field measurements, analyzed the measured spectra and conducted the design study of the camera system. T.L., J.P. and S.K. supported the design study of the camera system. T.L. wrote a section of the manuscript. D.B., D.E., M.D. and C.C. conducted the field measurements and supported the analysis of the measured spectra. M.D. wrote a section of the manuscript. All authors reviewed the manuscript. All authors read and approved the final manuscript.

**Funding** Open Access funding enabled and organized by Projekt DEAL. The ROMEO development of the core avionics, as well as the phases C and D are supported by the Federal Ministry for Economic Affairs and Climate Action of Germany via the German Space Agency at DLR (50RU2102 and 50RU2200). The flight hardware of the satellite is supported by the German Research Society (DFG) (INST 41/1139-1 FUGG). The measurements of the sugar beet spectra were organized and supported by the CORAmaps GmbH, the Nordzucker AG and the Martin Luther University Halle-Wittenberg. Apart from the mentioned fundings, the authors have no relevant financial or nonfinancial interests to disclose.

**Data availability** The measured spectra of sugar beets are provided within the manuscript via differences between healthy and diseased plants. The raw data of the measured spectra are available on demand via the corresponding author.

## **Declarations**

**Conflict of interest** The design study of the ROMEO satellite is supported by the Federal Ministry for Economic Affairs and Climate Ac-



tion of Germany via the German Space Agency at DLR and by the German Research Society (DFG) as declared in the authors section.

Open Access This article is licensed under a Creative Commons Attribution 4.0 International License, which permits use, sharing, adaptation, distribution and reproduction in any medium or format, as long as you give appropriate credit to the original author(s) and the source, provide a link to the Creative Commons licence, and indicate if changes were made. The images or other third party material in this article are included in the article's Creative Commons licence, unless indicated otherwise in a credit line to the material. If material is not included in the article's Creative Commons licence and your intended use is not permitted by statutory regulation or exceeds the permitted use, you will need to obtain permission directly from the copyright holder. To view a copy of this licence, visit http://creativecommons.org/licenses/by/4.0/.

## References

- Bundesanstalt fuer Geowissenschaften und Rohstoffe. Multispektrale Multisensor-Fernerkundung. URL: https://www.bgr.bund.de/ DE/Themen/GG\_Fernerkundung/Multispektrale\_Fernerkundung/multispektrale\_FE\_node.html. Accessed 27 Jul 2023.
- Fischer, C., Brunn, A.: Erfassung bergbaubedingter Veraenderung von Vegetationsparametern durch Nutzung hyperspektraler Bilddaten. Publikationen der Deutschen Gesellschaft fuer Photogrammetrie, Fernerkundung und Geoinformation e.v., 12, 211–219 (2003)
- 3. Ehlert, I., Schweitzer, C.: Copernicus fuer das Umweltmonitoring. Eine Einfuehrung, (2018)
- IPPC Secretariat. Scientific review of the impact of climate change on plant pests. FAO on behalf of the IPPC Secretariat, Rome, Italy, 2021. https://doi.org/10.4060/cb4769en
- Bundesverband der Deutschen Industrie e.V. NewSpace Initiative. URL: https://bdi.eu/themenfelder/sicherheit/newspace-initiative/. Accessed 27 Jul 2023.
- Kleinsatelliteninitiave deutscher Hochschulen. Kleinsatelliteninitiative deutscher Hochschulen. URL: www.kleinsatelliteninitiative.de. Accessed 27 Jul 2023.
- Union of Concerned Scientists. UCS Satellite Database. URL: https://www.ucsusa.org/resources/satellite-database. Accessed 27 Jul 2023.
- European Commission. Sugar. URL: https://agriculture.ec.europa. eu/farming/crop-productions-and-plant-based-products/sugar\_en. Accessed 27 Jul 2023.
- Britannica. Sugar Beet. URL: https://www.britannica.com/plant/ sugar-beet. Accessed 27 Jul 2023.
- European Association of Sugar Manufacturers. CEFS Statistics 2020/21. URL: https://cefs.org/wp-content/uploads/2022/04/ CEFS-Statistics-2020-2021.pdf. Accessed 27 Jul 2023.
- Schubinger, F. X.: Cercospora-Blattflecken. URL: https://www. pflanzenkrankheiten.ch/krankheiten-an-kulturpflanzen-2/weitereackerkulturen/zuckerrueben/cercospora-beticola. Accessed 27 Jul 2023
- Kuratorium fuer Versuchswesen und Beratung im Zuckerruebenanbau. Blatt-Krankheiten. URL: https://bisz.suedzucker.de/ flanzenschutz/blatt-krankheiten/. Accessed 27 Jul 2023.
- Institut fuer Zuckerruebenforschung. Erzeugung von rezessiver Resistenz gegenueber Blattlaus-uebertragbaren Vergilbungsviren der Zuckerruebe als Alternative zur chemischen Vektorkontrolle. URL: https://www.ifz-goettingen.de/index.php/de/navigation/ forschung/itemlist/category/373-vergilbungsviren.html. Accessed 27 Jul 2023.

- Spectral Evolution. RS-3500 Remote Sensing Portable Spectroradiometer Bundle. URL: https://spectralevolution.com/products/ hardware/field-portable-spectroradiometers-for-remote-sensing/ rs-3500/. Accessed 27 Jul 2023.
- Turpie, K.: Explaining the spectral red-edge features of inundated marsh vegetation. J. Coast. Res. 29, 1111–1117 (2013). https://doi.org/10.2112/JCOASTRES-D-12-00209.1
- Gates, D., Keegan, H., Schleter, J., Weidner, V.: Spectral properties of plants. Appl. Opt. 4(1), 11–20 (1965). https://doi.org/10.1364/AO.4.000011
- Schmittgen, S.: Effects of Cercospora leaf spot disease on sugar beet genotypes with contrasting disease susceptibility. PhD thesis, Heinrich-Heine-Universitaet Duesseldorf, Duesseldorf, Germany, (2014)
- The European Space Agency. Resolution and Swath. URL: https://sentinels.copernicus.eu/web/sentinel/missions/sentinel-2/instrument-payload/resolution-and-swath. Accessed 27 Jul 2023.
- Ganushkina, N., Dandouras, I., Shprits, Y., Cao, J.: Locations of boundaries of outer and inner radiation belts as observed by Cluster and Double Star. J. Geophys. Res. 116, 18 (2011). https:// doi.org/10.1029/2010JA016376
- Hildebrandt, J., Vikas, A., Loeffler, T., Fasoulas, S., Herdrich, G., Klinkner, S.: Satellite Water Propulsion: 3D Printed Ceramic Thruster & Space Debris Mitigation Concept. Aerospace Europe Conference 2023, Lausanne, Switzerland, (2023)
- Loeffler, T., Burgdorf, J., Klinkner, S.: Orbit-raising strategies for cost-efficient access to lower Medium Earth Orbit without risking space debris. Acta Astronaut. 185, 37–41 (2021). https://doi.org/ 10.1016/j.actaastro.2021.04.041
- Loeffler, T., Burgdorf, J., Hildebrandt, J., Boetsch-Zavřel, L., Holeczek, C., Paetschke, S., Kanzow, M., Largent, P., Petri, J., Lengowski, M., Klinkner, S.: Preliminary Design of the Radiation Protection of the ROMEO Satellite in the lower Medium Earth Orbit. 73rd International Astronautical Congress, Paris, France, (2022)
- 23. Waizenegger, K., Löffler, T., Burgdorf, J., Acker, D., Bötsch-Zavřel, L., Eggert, M., Hildebrandt, J., Holeczek, C., Kanzow, M., Konieczny, D., Lengowski, M., Mohr, U., Nehlich, P., Schweigert, R., Starzmann, D., Steinert, M., Vikas, A., Vossoughi, B., Zink, J., Klinkner, S.: System design phase C of the satellite ROMEO for the inner radiation belt of the medium earth orbit. In: 75th International Astronautical Congress, 10 (2024)
- Waltham, N.: CCD and CMOS sensors. ISSI Sci. Rep. Ser. 9, 391–408 (2010)
- Walz, S.: Nutzlast des Kleinsatelliten Flying Laptop. PhD thesis, University of Stuttgart, Stuttgart, Germany, (2011)
- Edmund Optics. Introduction to Modulation Transfer Function. URL: https://www.edmundoptics.eu/knowledge-center/application-notes/optics/introduction-to-modulation-transfer-function/. Accessed 27 Jul 2023.
- Schott, A.G.: TIE-42 Radiation Resistant Optical Glasses. URL: https://www.schott.com/shop/medias/schott-tie-42-radiation-resistant-optical-glasses-row.pdf. Accessed 27 Jul 2023.
- Gusarov, Andrei I., Doyle, Dominic, Hermanne, Alex, Berghmans, Francis, Fruit, Michel, Ulbrich, Gerd, Blondel, Michel: Refractive-index changes caused by proton radiation in silicate optical glasses. Appl. Opt. 41(4), 678–684 (2002). https://doi.org/10.1364/AO.41.000678
- Ferguson, Henry C., Dickinson, Mark, Williams, Robert: The Hubble deep fields. Ann. Rev. Astron. Astrophys. 38(1), 667–715 (2000)
- Bertaux, J.L., Lallement, R., Ferron, S., Boonne, C., Bodichon, R.: TAPAS, a web-based service of atmospheric transmission computation for astronomy. Astron. Astrophys. 564, 46 (2014). https://doi.org/10.1051/0004-6361/201322383



- 31. Simera Sense (Pty) Ltd. xScape100 Product Range. URL: https://simera-sense.com/products/xscape100-2/. Accessed 27 Jul 2023.
- 32. KAIROSPACE Co. Ltd. Kairospace Delivering Space. URL: http://kairo.space. Accessed 27 Jul 2023.

**Publisher's Note** Springer Nature remains neutral with regard to jurisdictional claims in published maps and institutional affiliations.

